An Ultrawideband Hybrid TEM-Horn Loop Circular Phased Array Enabled by Lens Loading

Edward Wawrzynek, Songyi Yen, and Dejan Filipovic
Department of Electrical, Computer, and Energy Engineering
University of Colorado Boulder
Boulder, CO, USA
{edward.wawrzynek, songyi.yen, dejan}@colorado.edu

***Abstract*—A method for increasing the instantaneous bandwidth of circular arrays by reducing under-sampling between elements is proposed. The method is applied to the design of a ten element TEM-horn loop circular array loaded with lenses which enable pattern synthesis when the array would otherwise be under-sampled. Through the quasi-conformal transformation optics, lenses are designed to reshape the near fields of each element to resemble those of a more tightly spaced array. This enables operation at high frequencies where the array would otherwise be affected by spatial aliasing and the radiation of harmonic distortion modes. The measured array achieves a combined impedance and pattern bandwidth of 6.5:1. Scanned operation is demonstrated with better than 11 dBi directivity and controlled sidelobes. Measurement of lens loading confirms its ability to reduce the amplitude of radiated harmonic modes and stabilize the array's characteristics over frequency.**

I. Introduction

Circular arrays find a wide range of applications, including those in communication, direction finding, and radar [1], [2]. These systems offer several advantages compared to linear or planar arrays. First, circular arrays offer the ability to realize a 360° degree scan in azimuth with minimal scan loss. Second, circular arrays can be operated in both omnidirectional and directional modes, which is useful in applications which require reconfigurability between wide-angle operation and the generation of a highly-targeted beam. Third, the generation and steering of multiple nulls in the radiation pattern can be realized through circular mode beamforming [3].

The bandwidth of circular arrays is limited primarily by element spacing. Elements must be close enough together to satisfy the $\lambda/2$ sampling criterion [2]. Insufficient spacing leads to the radiation of spatially aliased harmonic modes, analogous to the grating lobes that appear in linear arrays with insufficient spacing. These aliased modes severely distort the radiation pattern of the array and make the realization of a single directive beam impossible. The spacing requirement is particularly restrictive for wideband operation: the sampling criterion must be satisfied at the highest frequency of operation, which corresponds to elements spaced electrically close together at the low frequencies of operation. Existing methods for wideband circular arrays have focused on lowering this low frequency limit, through the use of tightly coupled elements [4]–[7] or electrically small elements [8], [9]. The high frequency limit of these arrays is typically constrained by this spacing requirement rather than by impedance bandwidth. Experimental demonstrations of circular phased arrays have not exceeded a 4:1 bandwidth [4]–[9]. Expanding on the theoretical method proposed in [10], this work demonstrates an increase in the high frequency limit by reconfiguring an existing array with lenses which distort the radiation patterns of the elements to meet the sampling criterion at higher frequency.

This work is funded by the Office of Naval Research under grant N00014-24-1-2191 and by the US Department of Defense.

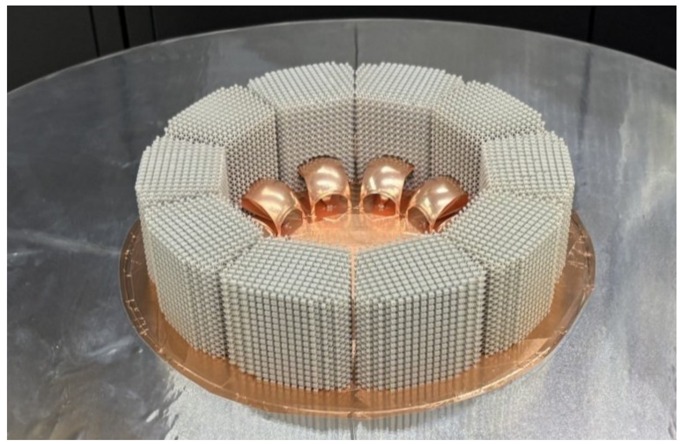

Fig. 1: A photograph of the proposed circular phased array, showing four of the ten TEM-horn loop elements surrounded by gradient index of refraction lenses. The array is mounted on a 110 cm ground plane for chamber measurement.

To achieve the desired sampling at high frequency, the lenses in this work are designed through transformation optics [11], [12]. In the transformation optics, the shape of a known electromagnetic device is transformed to a different shape while retaining the electromagnetic field distribution through modified permittivity and permeability of the surrounding space.

In general, the resulting permittivity and permeability are anisotropic and therefore hard to fabricate in a broadband manner. If the transform used is uniform in one dimension and conformal in the other two, the resulting materials simplify to those of a uniaxial media. In the quasi-conformal transformation optics (QCTO), transforms are selected to be nearly conformal and the uniaxial media approximated by a purely dielectric implementation, which enables broadband devices [11].

In antenna design, transforms are typically selected to distort the near fields of an antenna to those which result in a more favorable far field pattern. This technique has been used to enhance antenna directivity through collimation [13], [14], generate multiple beams from an omnidirectional source [15], and reshape the pattern of a conformal array into that of a linear array [16].

To practically demonstrate the proposed concept, a circular array shown in Fig. 1 is designed and fabricated. The array consists of ten hybrid TEM-horn loop elements surrounded by gradient index lenses. The lenses flatten the phase front radiated by each element, moving the element's phase centers towards the center of the array. This reduces the radiation of high order circular phase modes and therefore improves pattern quality at high frequency.

This paper is organized as follows: Section II briefly reviews the theory of circular arrays and the source of harmonic mode radiation. Section III discusses the design of the lenses through QCTO and their fabrication. Section IV presents the design of the array elements and their integration with the lenses, while Section V discusses the measured array performance. Section VI concludes the paper.

II. Circular Arrays

The behavior of the array is studied through circular phased modes [1], [2]. Circular phase modes are a natural basis for circular arrays, since they closely correspond to both the cylindrical waves radiated by the array in the spatial domain and to the eigenvectors of the array's scattering parameters in the circuit domain.

To start, the far field pattern of the array is expanded into a Fourier series of circular phase modes with coefficients A_m,

$$E(\phi) = \sum_{n=-\infty}^{\infty} A_m e^{jm\phi}. \tag{1}$$

Because (1) takes the same form as the relationship between port excitation and the far field of a linear array, the circular modes are analogous to port excitation of a linear array. Maximum directivity is achieved with uniform circular mode excitation, scanning is achieved by increasing the phase of successive modes, and tapering can be applied to control side-lobes. However, the relationship between the circular modes and port excitations is more complicated than in a linear array.

If the embedded element pattern is expanded (with the element at the origin) in a Fourier series

$$EL(\phi) = \sum_{p=-\infty}^{\infty} D_p e^{jp\phi}, \tag{2}$$

then the amplitude of the m-th mode in far field (A_m) is related to the amplitude at the array elements (C_m) as [1]

$$\frac{A_m}{C_m} = \sum_{p=-\infty}^{\infty} D_p j^{m-p} J_{m-p}\left(k_0 r\right), \tag{3}$$

where r is the radius of the array, k_0 is the free space wavenumber, and J_l is the Bessel function of the first kind.

Equation (3) relates the amplitude of the desired mode in far field and near field. However, the array is excited at N discrete ports. For modes C_m, the corresponding voltage on the n-th port is

$$V_n = \sum_{m=-\infty}^{\infty} C_m e^{j2\pi mn/N}. \tag{4}$$

For the ten element array in this work, only ten distinct phase modes can be excited, $m = -5$ to $m = 5$, where the $m = -5$ and $m = 5$ modes are degenerate with each other.

However, excitation of the m-th mode on the array port also excites all of it's harmonics, C_{m-N}, C_{m+N}, C_{m-2N}, C_{m+2N}, etc. If radiated into the far field, these harmonic modes disrupt the synthesis of a desired pattern. How strongly these harmonic modes radiate into the far field is determined by the windowing behavior of the Bessel functions in (3), which is a function of the electrical radius $k_0 r$ at which they are excited and the spectral content D_p of the element pattern. This is similar to the emergence of grating lobes in under-sampled linear arrays. The transition of harmonic modes from being largely reactive and non-radiative to being radiative at higher frequencies is broadly analogous to the notion of grating lobes moving from the invisible to visible space in a linear array. The lenses in this work are designed to tailor the spectral content of the element pattern to reduce the strength of harmonic radiation.

III. Lens Design

The lenses are designed to flatten the phase front of an array element and therefore move the apparent element phase center closer to the physical center of the array. The transformation domains are shown in Fig. 2. The virtual domain, Fig. 2(a), is mapped to the physical domain, Fig. 2(c). The virtual domain has a point source embedded in its center and its upper boundary is a circular arc centered on this source. This boundary is intended to capture a portion of the circular phase front radiating from the source. In the physical domain, this arc is mapped to a circular arc with a larger radius of curvature. This physical arc is selected to have a center located behind the source location, which corresponds to a flattening of the phase front from the virtual space to the physical space. The wave radiated from the lens, therefore, appears to have originated from a source located behind the physical location of the source. In an array setting, this will be used to realize element phase centers located closer to the center of the array than the physical elements.

The shape of the physical domain is fixed by the requirement that the lenses can be placed in a circular array, which necessitates the use of a wedge-shaped domain which can be revolved and tiled in a circular pattern. For practical verification of the theory, a ten element array is selected, which constrains each physical domain to a 36° wedge. The intersection angle between the circular arc and the vertical edges in the virtual and physical domains are matched to each other to avoid singularities in the resulting conformal map.

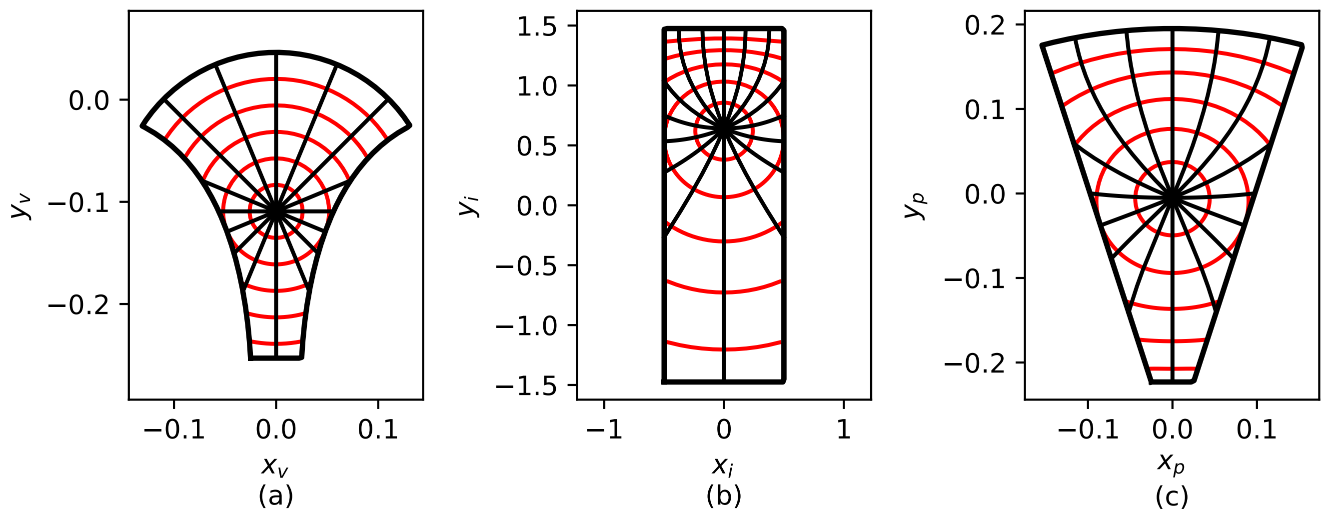

Fig. 2: Transformation domains under consideration, plotted with a grid undergoing the conformal transform between them. The domains are (a) the virtual domain, (b) the intermediate domain, and (c) the physical domain.

The shape of the vertical edges in the virtual space are selected to tailor the resulting permittivity distribution, which will be examined later.

A. Optical Path Rescaling

Two quasi-conformal transforms are found numerically from the virtual and physical domains to the intermediate domain, similar to the method described in [17]. Usage of a rectangular intermediate domain, shown in Fig. 2(b), allows these transforms to be found as the solution to a linear boundary value problem [17]. The transform from the physical domain to the intermediate domain is numerically inverted and composed with the transform from the virtual to intermediate domain, yielding the full transform from the virtual to physical domain. The resulting permittivity distribution is computed as in [11].

The domains are tuned to have well matched conformal moduli, with an anisotropy factor $\alpha \approx 1.005$, suggesting that the transform is highly isotropic. The resulting permittivity profile is shown in Fig. 3(a). The profile contains both subluminal ($\epsilon_r \geq 1$) and superluminal ($\epsilon_r < 1$) regions. In order to realize a broadband design, these superluminal areas are removed through optical path rescaling [18]. As a wave travels outwards from some point source within the lens, it accumulates some phase $\psi(\rho)$. Locally, this accumulated phase must satisfy an Eikonal equation,

$$|\nabla\psi(\rho)| = \sqrt{\epsilon_r(\rho)}k_0. \tag{5}$$

Since the QCTO realizes permittivity distributions which are almost reflection-free, (5) is a good approximation of both the classical geometric optics from which it is derived and of the full physical wave optics of the lens.

Optical path rescaling is based on the observation that solutions to (5) are invariant under smooth changes to $\epsilon_r(\rho)$ along iso-curves of $\psi(\rho)$. For some monotonic rescaling function $S(\psi)$, the scaled permittivity is

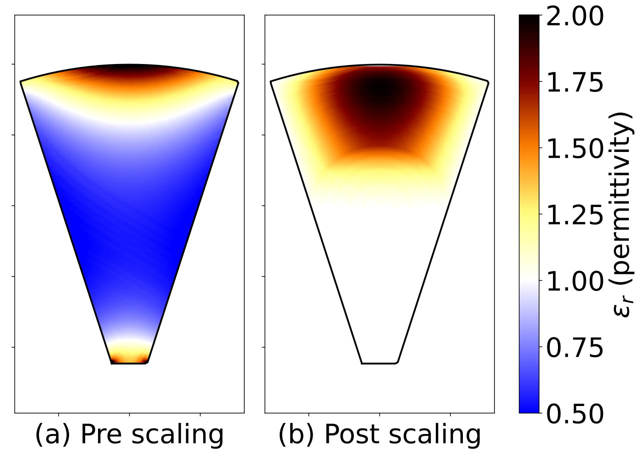

Fig. 3: Permittivity profile of a lens element corresponding to the transform of Fig. 2, (a) before and (b) after optical path rescaling.

$$\epsilon_r^* = \epsilon_r \left|\frac{\mathrm{d}S}{\mathrm{d}\psi}\right|^2. \tag{6}$$

This rescaling process (6) corresponds to uniformly scaling the permittivity along curves of constant phase. For the considered lenses, example curves of constant phase are marked in red in Fig. 2. The rescaling function is selected to yield a minimum permittivity of $\epsilon_r^* = 1$,

$$S(\psi) = \max_{c\,\in\,C} \int_{c=0}^{\psi} \frac{1}{\sqrt{\epsilon_r(\rho)}}\mathrm{d}s, \tag{7}$$

where C is the set of all ray paths through the lens. The rescaled permittivity of the lens is plotted in Fig. 3(b), showing the elimination of the superluminal regions. Additionally, the

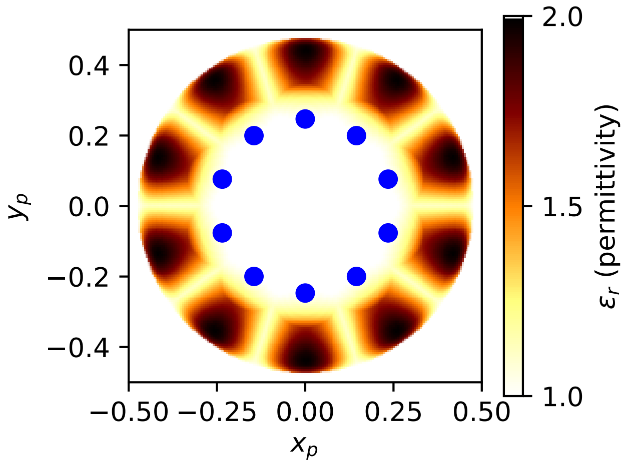

Fig. 4: Permittivity profile of the full ten element lens array. The design location of sources are marked by blue dots.

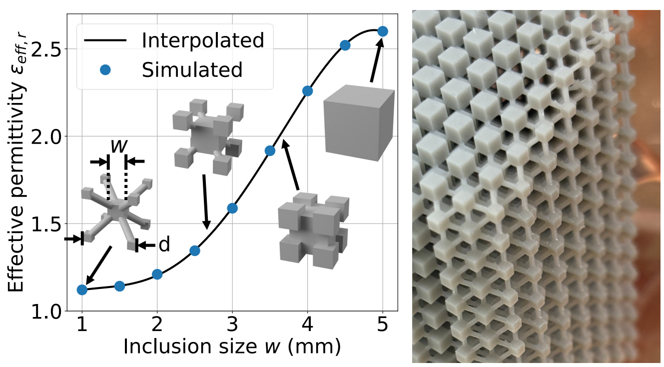

(a) (b)

Fig. 5: Realization of the gradient index lens, showing (a) the effective permittivity of the lens unit cells at 8 GHz for varying inclusion widths w and (b) a portion of a fabricated lens. The figures inset in (a) show representative unit cell geometries as the inclusion width is swept.

side profiles of the virtual domain are tailored to give the bottom half of the rescaled lens a permittivity close to that of free space. Since this region of the lens is well approximated by air, this is useful for the placement of source elements within this region.

The lens arrangement is formed from ten individual lens elements rotated to form a circular array. The total permittivity profile of the array is shown in Fig. 4, where the sources are located at the positions of the virtual antennas transformed into the physical space. The permittivity profile is extruded uniformly upward to a height of 80 mm. The lens height is chosen to capture at least a significant portion of a wavelength at the frequencies where aliasing effects become significant.

B. Gradient Index Lens Design

The gradient permittivity of the lens is realized through a discrete quasi-periodic lattice. The lattice consists of repeated unit cells that have a slow variation in their geometric parameters. This variation corresponds to the desired spatially varying permittivity.

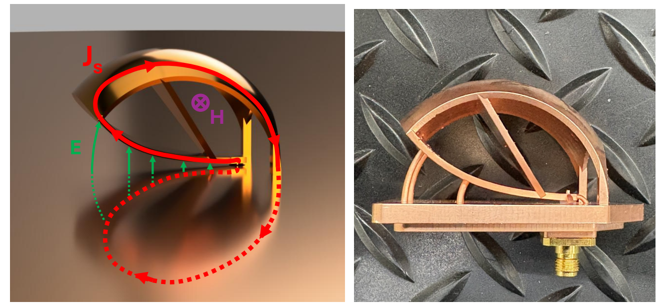

(a) (b)

Fig. 6: The hybrid TEM horn-loop element used in the array, showing (a) the operating principle of the element and (b) a fabricated element prior to plating support removal. In (a), the red arrows denotes surface currents along the antenna, which create the electric dipole in the horn (green) and magnetic dipole in the loop (purple). The dashed traces are equivalent image currents and fields below the ground plane.

The unit cell of the lattice is shown in Fig. 5. The unit cell is formed from a central cubical inclusion connected to the eight diagonally neighboring cubes by a cylindrical support, forming a body centered cubic lattice. The total unit cell length is $d = 5$ mm, while the central cube has width w which is swept from $w = 1$ mm to $w = d = 5$ mm. The cylindrical supports between cubes have diameter $(1\ \text{mm}/\sqrt{2}) \approx 0.707$ mm. When the inclusion is large enough to intersect it's neighbors, $w > 3$ mm, the cylindrical supports are not needed.

Fig. 5 shows the effective permittivity of the unit cell as a function of w. The effective permittivity is determined from Floquet analysis of an infinite lattice of cells, simulated numerically with Ansys HFSS. Since the unit cell is electrically small ($d = 0.15\lambda$ at highest frequency of operation), the lattice is expected to be highly isotropic [19].

To construct the discrete lattice, the continuous permittivity distribution of Fig. 4 is sampled at the lattice sites and the corresponding inclusion w is chosen based on the sweep in Fig. 5. The lenses are fabricated through stereolithographic 3d-printing in Arkema PR221 photoresin [20]. PR221 has a bulk permittivity of $\epsilon_r = 2.6$, while the lens requires a peak permittivity of $\epsilon_{r,max} \approx 2.0$, so the cube size peaks at $w \approx 3.8$ in the densest part of the lens. The unit cell can only realize effective permittivity down to $\epsilon_r \approx 1.14$ due to the dielectric taken by the supporting cylinders, so the regions of the profile with ϵ_r below 1.14 are replaced with air. The body centered cubic lattice gives each unit cell eight connections to its neighbors, which results in a mechanically robust structure during and after printing.

IV. Array Design

The proposed lens loading technique is general and can be applied to many different types of array elements. In this work, the array is realized from hybrid TEM-horn loop elements, which are selected due to their wide impedance bandwidth, small electrical size at turn-on, and relatively stable phase center [21].

The TEM-horn loop antennas are similar in design and dimension to those described in [22]. The TEM-horn loop design is shown in Fig. 6. The element is realized on a ground plane and the TEM-horn section is fed by a coaxial pin connector through the ground plane. The TEM-horn section transitions into a loop surface which travels backwards from the horn and bifurcates into two posts which contact the ground. A slanted bowtie is included between the horn and loop sections. At high frequency, the antenna's characteristics are dominated by the TEM horn. At low frequency significant currents make it past the end of the horn section and additionally excite the loop mode. In this mode, the antenna is designed to excite both an electric and magnetic dipole, where the electric dipole is formed from the horn and bowtie and the magnetic dipole is formed from the loop [21]. Together these dipoles realize a Huygens-source like pattern with radiation directed in the direction of the horn. Compared to [22], the element in this work has a forward slanted bowtie, which improves mid frequency impedance matching.

The elements of the array are stereolithographically 3d-printed in Arkema PR221 photoresin [20] and copper electroplated. The elements are laid out in a circular array with an outer radius of 104 mm. Lenses are placed around the array, with small cutouts for the front sections of the elements, visible in Fig. 1. With lenses, the total array radius is 160 mm. The array is placed on a 550 mm radius ground plane for measurement.

V. Performance

The array's performance is simulated in HFSS, with the lens geometry represented by a continuous permittivity distribution. The measured and simulated passive reflection coefficients of each element are shown in Fig. 7. The passive element turn-on is consistent between simulation and measurement, reaching 10 dB return loss at 1.7 GHz, and the elements remain matched through 10 GHz.

The array is scanned by exciting the phase modes with a progressive phase shift given by the desired scan direction. The amplitudes of the phase modes are weighted with a -20dB Taylor taper intended to reduce the sidelobe level. The port excitations are given by (3) and (4) in terms of the desired far field amplitude.

The range of active reflection coefficient of each element when the array is scanned across the entire 360° azimuth plane is shown in Fig. 8. Also plotted is the total active reflection coefficient (TARC), defined as

$$\Gamma_{total} = \sqrt{\frac{\sum_n |b_n|^2}{\sum_n |a_n|^2}}, \tag{8}$$

which captures the proportion of power incident on the array ports which is reflected. The measured TARC reaches -6dB near 1.3 GHz, defining the lower range of the impedance bandwidth. The active reflection coefficient displays more inter-element variation at low frequencies due to higher mutual coupling between elements.

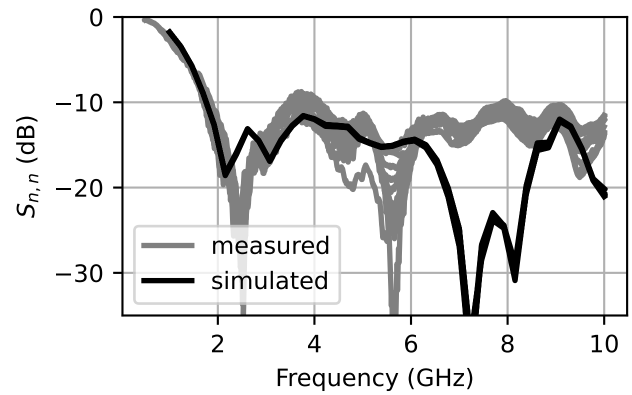

Fig. 7: Simulated (black) and measured (gray) passive reflection coefficients of each element in the array. The range of gray traces shows inter-element variation.

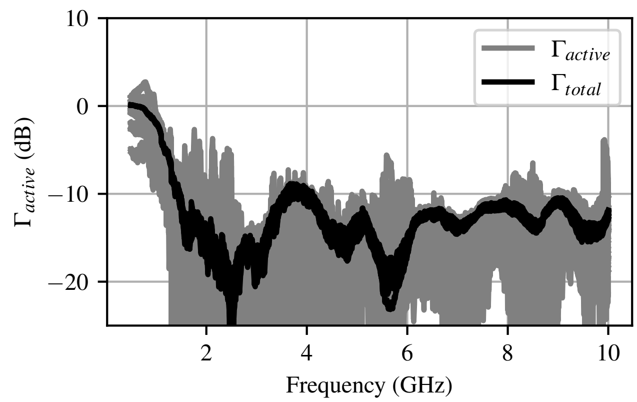

Fig. 8: Measured active reflection coefficient of array elements when scanning across the entire 360° azimuth plane. The gray traces show the range of per-element active reflection coefficients, while the black traces show the range of the total active reflection coefficient.

A. Array Patterns

The simulated beamformed patterns of the array are shown in Fig. 9 across a 9:1 bandwidth. As seen, patterns are plotted with the scan direction centered. Both the array without and with lens loading achieve well controlled patterns at low frequency (at and below 3 GHz). The main lobe shows little variation under different scan angles, although sidelobes are slightly elevated when scanning between elements. At low frequency the elements are spaced closely enough electrically to avoid any significant excitation of harmonic circular phase modes, and the modes excited on the ports of the array are those which radiate into the far field. This allows for well controlled pattern synthesis.

Without lens loading, the element spacing becomes electrically large at higher frequency and the system suffers from the effects of radiating harmonic modes. The sidelobe level

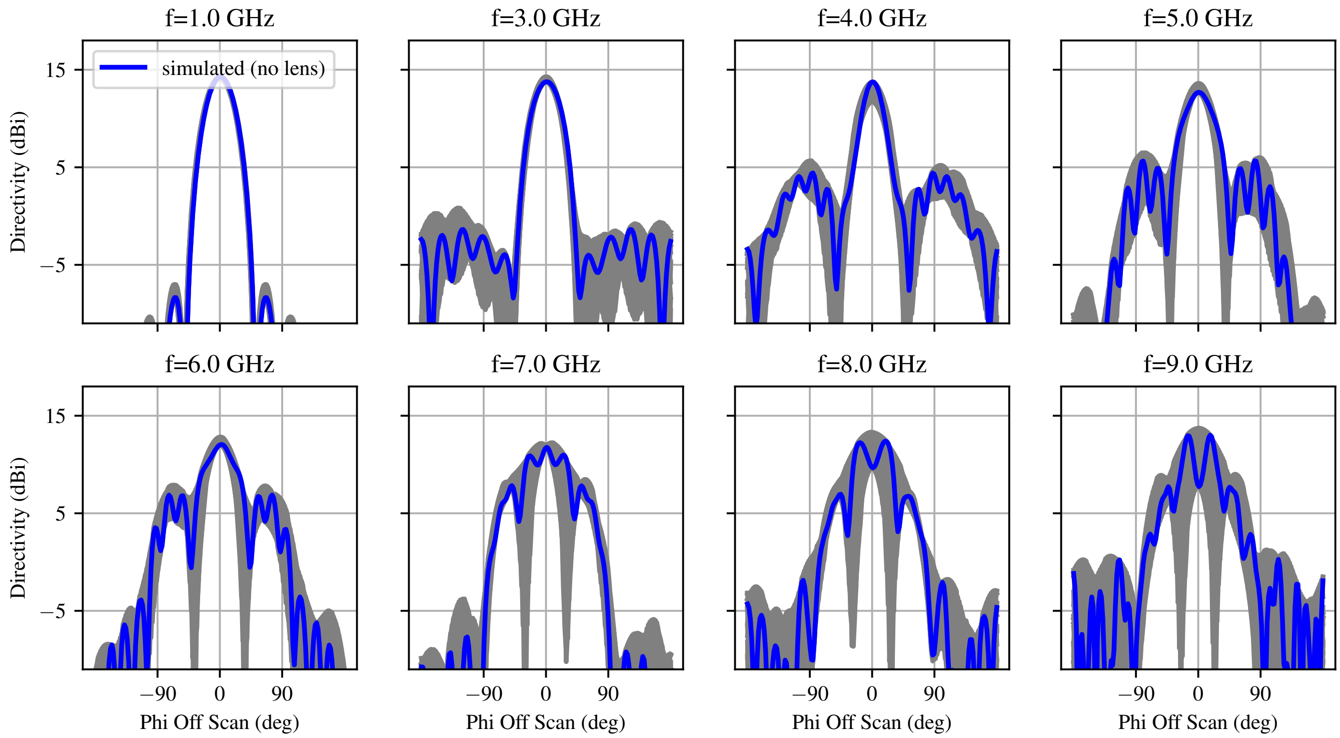

(a)

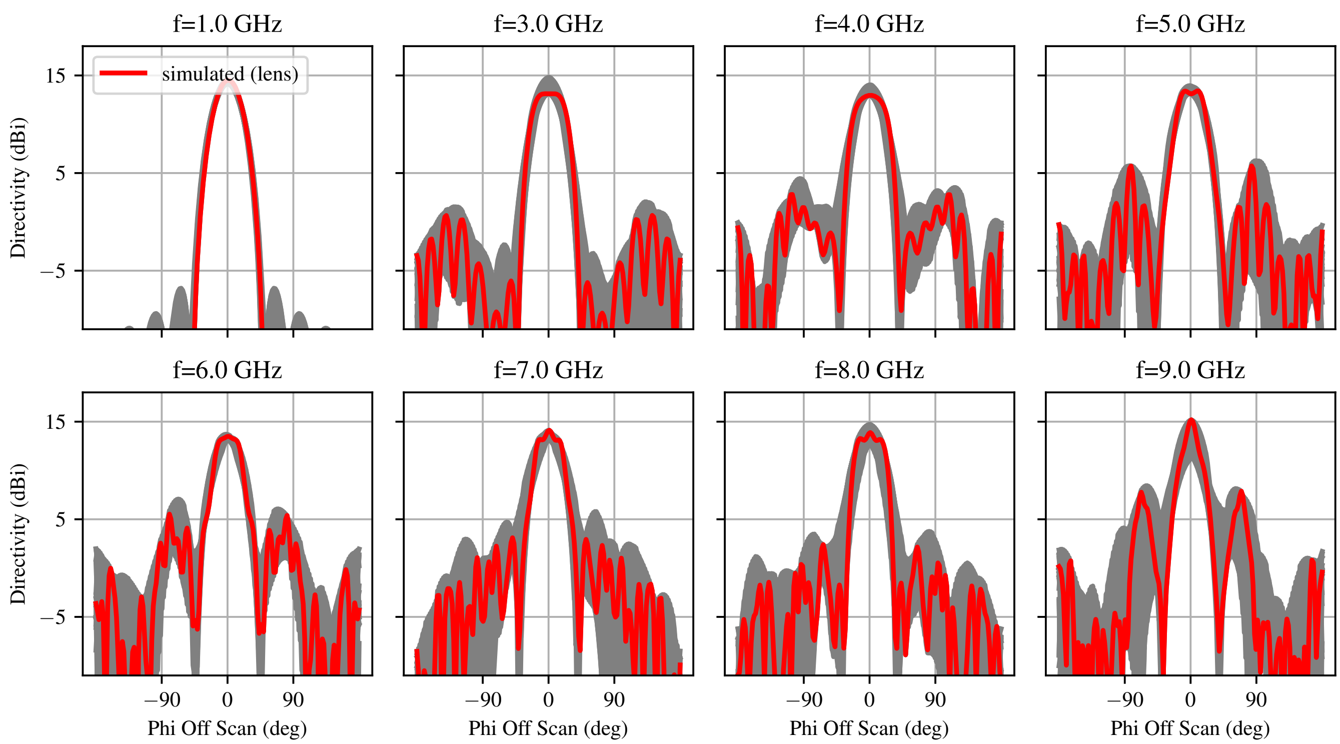

(b)

Fig. 9: Simulated H-plane (at $\theta = 90°$) beamformed patterns of the array, (a) without and (b) with lenses present. Each pattern is plotted with the scan direction centered. Solid traces show the pattern when scanned in the direction of an element, while gray traces show variability as the pattern is scanned between elements.

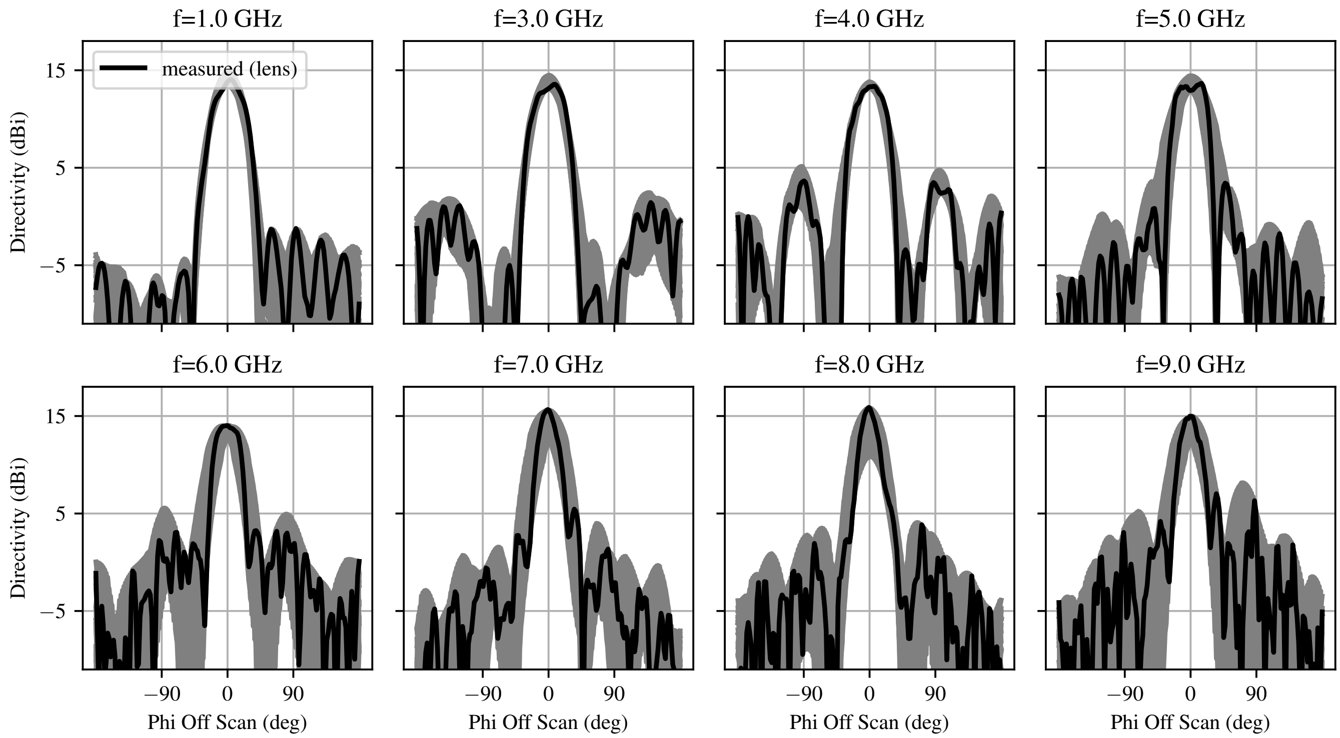

Fig. 10: Measured H-plane (at $\theta = 90°$) beamformed patterns of the array with lenses present. Each pattern is plotted with the scan direction centered. Black traces show the pattern when scanned in the direction of an element, while gray traces show variability as the pattern is scanned between elements.

increases significantly, causing the peak mainbeam directivity to drop notably. At 7 GHz and above the main beam begins to show significant pattern variation while scanning and the difference between the main beam and side lobes becomes hard to clearly identify.

With lens loading, however, the array maintains better control of the pattern at higher frequency. The sidelobe level is reduced, staying under -8 dB from the mainbeam below 8.6 GHz. The worst-case directivity of the mainbeam is stabilized to within 3dB of the low frequency beam until 8.8 GHz, and overall beam variability during scanning is reduced.

The measured beamformed patterns of the array with lenses are shown in Fig. 10. Only five of the ten embedded element patterns were measured, with the total pattern of synthesized by duplicating the five measured patterns about the center of the array. The measured patterns of the array are similar to those simulated, and the same qualitative conclusions regarding the effects of lens loading can be seen. At high frequency (above 5 GHz) the measured array has slightly narrower element patterns than the simulated array, leading to higher beamformed directivity at the expense of higher beam variability when scanning. Sidelobe behavior is slightly better in measurement than simulation, remaining -8 dB below the mainbeam through 8.5 GHz. Taken together with the TARC turn on of 1.3 GHz, this is a measured bandwidth of 6.5:1. Without lenses, the same pattern metrics are achieved only through 4.8 GHz, a bandwidth of 3.7:1, similar to that observed in other TEM-horn arrays [8]. This suggests that lens loading of circular arrays is a viable approach to expand the upper limit of usable pattern bandwidth.

B. *Distortion Reduction*

The effect of the lenses on radiation of harmonic circular phase modes can be studied through the distortion ratio, defined here for the m-th mode as the far field power in harmonic modes relative to far field power in the desired m-th fundamental mode,

$$\Delta_m = \frac{\sum_{n \neq m} |A_n|^2}{|A_m|^2}. \tag{9}$$

The distortion ratio for the (measured) array with lenses compared to the (simulated) array without lenses is shown in Fig. 11. The distortion ratio is low at low frequencies, since the elements are tightly spaced and harmonic modes are poorly radiated. At low frequency the lenses increase the distortion ratio. This is attributable to the larger electrical size of the total equivalent aperture when lenses are present and the correspondingly higher efficiency with which harmonic modes radiate from the larger aperture. However, the distortion ratio is low with or without lenses at low frequency.

As frequency increases and elements become insufficiently spaced, harmonic modes are more efficiently radiated, and the distortion ratio increases. Above 4 GHz, the lenses decrease distortion. This reduction is most significant in the lower

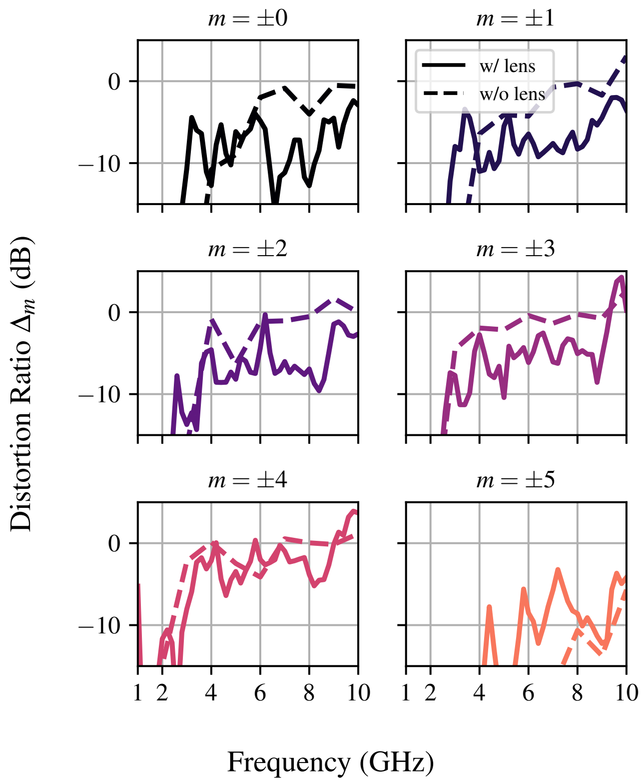

Fig. 11: Distortion ratio of each circular mode in the array with and without lenses. The distortion ratio with lenses is taken from measured patterns while that without is taken from simulation.

order modes, although all modes through $m = \pm 4$ see some level distortion reduction between 6 GHz and 8.5 GHz. This reduction is responsible for the improvements in pattern quality seen in Fig. 9 and 10.

VI. Conclusion

This work demonstrates that the pattern bandwidth of circular arrays can be extended by dielectric lens loading. The lenses are designed to distort the near fields of an under-sampled array to appear as though the array is sufficiently sampled. This distortion is achieved by moving the phase center of the array elements inwards, making the elements appear more closely packed together electrically than their physical locations.

Lenses are designed, fabricated, and measured loading a ten element hybrid TEM-horn loop circular phased array. Measurement demonstrates that lens loading reduces the proportion of power which radiates in aliased harmonic circular phase modes when the array is under-sampled. This reduction in harmonic mode radiation corresponds to improvements in synthesized pattern quality and stability over frequency. Applied to the TEM-horn loop array, lens loading is shown to extend the usable array bandwidth from 3.7:1 to 6.5:1.

Acknowledgment

The authors thank Isaiah Pisani, Benjamin Cross, and Ljubodrag Boskovic for useful discussions and assistance.

References

[1] D. Davies, "Circular arrays," *The handbook of antenna design*, vol. 2, pp. 299–329, 1983.

[2] L. Josefsson and P. Persson, *Conformal array antenna theory and design*. John wiley & sons, 2006.

[3] M. J. Radway and D. S. Filipovic, "Adaptive pattern nulling method for multi-armed spiral antennas," in *2010 IEEE Antennas and Propagation Society International Symposium*. IEEE, 2010, pp. 1–4.

[4] J. T. Logan, W. M. Dorsey, and J. A. Valenzi, "Modular all-metal ultrawideband cylindrical array for multifunction operation," *IEEE Trans. Antennas Propag.*, vol. 70, no. 10, pp. 9175–9183, 2022.

[5] X. Lv, Y. Zhang, Q. Shi, M. Temiz, and A. El-Makadema, "A dual slant-polarized cylindrical array of tightly coupled dipole antennas," *IEEE Access*, vol. 10, pp. 30 858–30 869, 2022.

[6] T. Yang, J.-C. Liang, R. Wang, J. Shao, Y. Wang, C. Zhang, and B.-Z. Wang, "Ultra-wideband 360° azimuthal continuous scanning radiator-sharing phased array," *IEEE Trans. Antennas Propag.*, 2025.

[7] Y. Hu, Y. Lu, K. Wang, L. Sun, Y. Li, Q. You, and Y. Wang, "Metallic dual-polarized cylindrical conformal phased array based on magnetoelectric dipoles," *IEEE Trans. Antennas Propag.*, 2025.

[8] M. A. Elmansouri, J. Ha, and D. S. Filipovic, "Ultrawideband TEM horn circular array," *IEEE Trans. Antennas Propag.*, vol. 65, no. 3, pp. 1374–1379, 2017.

[9] Z. Wang, P. S. Hall, J. R. Kelly, and P. Gardner, "Wideband frequency-domain and space-domain pattern reconfigurable circular antenna array," *IEEE Trans. Antennas Propag.*, vol. 65, no. 10, pp. 5179–5189, 2017.

[10] E. Wawrzynek, S. Yen, and D. Filipovic, "Bandwidth expansion of circular phased arrays through quasi-conformal transformation optics," in *2026 IEEE International Symposium on Antennas and Propagation and North American Radio Science Meeting (AP-S/CNC-USNC-URSI)*. IEEE, [in press].

[11] J. B. Pendry, D. Schurig, and D. R. Smith, "Controlling electromagnetic fields," *Science*, vol. 312, no. 5781, pp. 1780–1782, 2006.

[12] U. Leonhardt, "Optical conformal mapping," *Science*, vol. 312, no. 5781, pp. 1777–1780, 2006.

[13] M. Ebrahimpouri and O. Quevedo-Teruel, "Bespoke lenses based on quasi-conformal transformation optics technique," *IEEE Trans. Antennas Propag.*, vol. 65, no. 5, pp. 2256–2264, 2017.

[14] H. Eskandari, J. L. Albadalejo-Lijarcio, O. Zetterstrom, T. Tyc, and O. Quevedo-Teruel, "H-plane horn antenna with enhanced directivity using conformal transformation optics," *Scientific Reports*, vol. 11, no. 1, p. 14322, 2021.

[15] Q. Wu, Z. H. Jiang, O. Quevedo-Teruel, J. P. Turpin, W. Tang, Y. Hao, and D. H. Werner, "Transformation optics inspired multibeam lens antennas for broadband directive radiation," *IEEE Trans. Antennas Propag.*, vol. 61, no. 12, pp. 5910–5922, 2013.

[16] D.-H. Kwon, "Quasi-conformal transformation optics lenses for conformal arrays," *IEEE Antennas Wireless Propag. Lett.*, vol. 11, pp. 1125–1128, 2012.

[17] Z. Chang, X. Zhou, J. Hu, and G. Hu, "Design method for quasi-isotropic transformation materials based on inverse laplace's equation with sliding boundaries," *Optics express*, vol. 18, no. 6, pp. 6089–6096, 2010.

[18] H. Eskandari and T. Tyc, "Controlling refractive index of transformation-optics devices via optical path rescaling," *Scientific Reports*, vol. 9, no. 1, p. 18412, 2019.

[19] S. Tretyakov, *Analytical modeling in applied electromagnetics*. Artech House, 2003.

[20] Colorado Photopolymer Solutions. (2026) PR221-LCD technical datasheet. [Online]. Available: https://www.cpspolymers.com/PR221-LCD TDS.pdf

[21] M. A. Elmansouri and D. S. Filipovic, "Miniaturization of TEM horn using spherical modes engineering," *IEEE Trans. Antennas Propag.*, vol. 64, no. 12, pp. 5064–5073, 2016.

[22] S. Yen, L. B. Boskovic, M. A. Elmansouri, and D. S. Filipovic, "Ultra-wideband directional electrically small antenna for UHF through C-band 5G and beyond 5G applications," *Microwave and Optical Technology Letters*, vol. 66, no. 1, p. e33751, 2024.